

Simulations of Disordered Matter in 3D with the Morphological Autoregressive Protocol (MAP): Water

Ata Madanchi¹, Michael Kilgour^{2,§}, Frederik Zysk³, Thomas D. Kühne³, Lena Simine^{2*}

Affiliations:

¹Department of Physics, McGill University, 3600 University St., Montreal, Quebec, H3A 2T8, Canada.

²Department of Chemistry, McGill University, 801 Sherbrooke St. W, Montreal, Quebec, H3A 0B8, Canada.

³Dynamics of Condensed Matter and Center for Sustainable Systems Design, Chair of Theoretical Chemistry, University of Paderborn, Paderborn33098, Germany

Corresponding author: Lena Simine lena.simine@mcgill.ca

[§]current affiliation: Department of Chemistry, New York University, New York City, New York, 10003, United States

ABSTRACT

Disordered molecular systems such as amorphous catalysts, organic thin films, electrolyte solutions, even water are at the cutting edge of computational exploration today. Traditional simulations of such systems at length-scales relevant to experiments in practice require a compromise between model accuracy and quality of sampling. To remedy the situation, we have developed an approach based on generative machine learning called the Morphological Autoregressive Protocol (MAP). The MAP provides computational access to mesoscale disordered molecular configurations at linear cost at generation for materials in which structural correlations decay sufficiently rapidly. The algorithm is implemented using an augmented PixelCNN deep learning architecture that we previously demonstrated produces excellent results in 2 dimensions for mono-elemental molecular systems. Here we extend our implementation to multi-elemental 3D and demonstrate performance using water as our test system in two scenarios: 1. liquid water, and 2. a sample with a small ice nucleus. We trained the model on small-scale samples of liquid water produced using path-integral molecular dynamics simulation including nuclear quantum effects under ambient conditions. MAP-generated water configurations are shown to accurately reproduce the properties of the training set and to produce stable and physically sound behaviors when used to initialize classical and quantum dynamical simulations. We expect our approach to perform equally well on other disordered molecular systems given a suitable training set.

INTRODUCTION

There are numerous examples of amorphous or strongly disordered systems that gave rise to decades of fruitful research or hold a terrific potential for future applications: amorphous silica¹, water², amorphous catalysts³, amorphous graphene⁴. Computational exploration of such systems is hindered by the need to simulate large numbers of particles in difficult-to-sample free energy landscapes. The steep rise in simulation cost with system size is typically referred to as the ‘exponential wall’ or the ‘curse of dimensionality’ and it is due to the fact that the configuration space volume and the necessary sampling increase exponentially with number of particles. State of the art simulation methods approach the problem of bridging the nano-to-meso gap through the development of enhanced-sampling techniques⁵⁻⁷, coarse-grained potentials⁸⁻¹⁰ and machine-learning force fields^{11,12}. They increase to some degree the range of systems that may be successfully modeled but here we pursue a different strategy. We sacrifice some of the generality by limiting applicability to the class of strongly disordered systems, and we gain a linear scaling (with the number of the generated grid-points) algorithm that produces well sampled molecular structures. If needed, the samples may reach the mesoscale, and if needed, the resolution may remain atomistic.

Inspired by the successes of applying machine learning to sampling challenges⁵⁻⁷, we have recently introduced an approach for the simulations of strongly disordered matter as an autoregressive protocol based on deep learning called the Morphological Autoregressive Protocol (MAP)^{13,14}. It takes advantage of the locality of structural correlations in amorphous or strongly disordered materials and extrapolates molecular configurations from small-scale samples to arbitrary sizes at linear cost, see Figure 1 for a conceptual summary. Previously, we have implemented the MAP for the case of 2D mono-elemental materials using a deep generative model called gated PixelCNN^{15,16} and applied it to simulations of quantum dot aggregates, and to a recently discovered topologically distinct amorphous variant of graphene^{13,17,18}. Here, we upgrade it to multi-elemental 3D disordered structures.

The idea behind the MAP is that a neural network trained on small (order of the structural correlation-length) samples of a material (Figure 1A), learns the conditional probability of presence/identity of atoms at a point in space given the ‘context’ of surrounding atoms (Figure 1B). We estimate the correlation length L_c using a radial distribution function (RDF)

$$g(r) = \frac{1}{N} \left\langle \sum_{i \neq j}^N \delta(r - r_{ij}) \right\rangle$$

where δ is the Dirac delta function, r the radius, r_{ij} the distance of particle j from the reference particle i , and N the total number of particles. The probability conditional on the context with the size of L_c is then sampled in an autoregressive fashion with newly generated points becoming input for further generation reducing the cost of simulation to linear scaling with sample size and opening access to large-scale well sampled configurations (Figure 1C). Using the MAP, the molecular structures are generated in a directional manner one grid-point at a time and the required input ‘molecular context’ is limited to the space directly preceding the generated grid-point. We found that ‘molecular context’ truncated in this fashion is sufficient for successful extrapolation in the case of 2D amorphous materials¹³ and here we show that it is indeed sufficient for the 3D case as well.

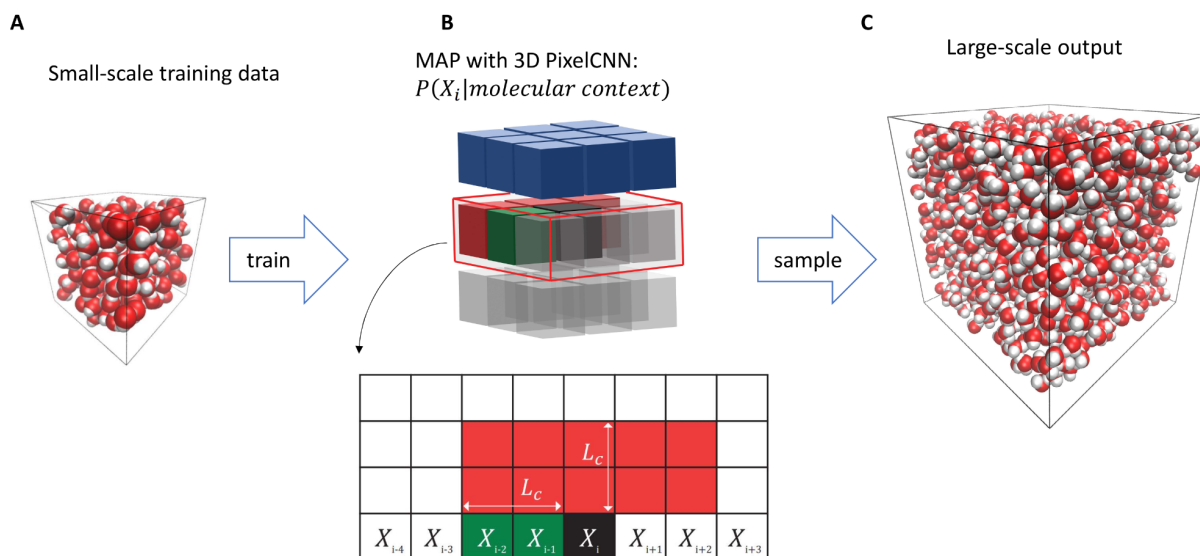


Figure 1: Workflow diagram for Morphological Autoregressive Protocol (MAP) in 3D. A. Training samples (size on the order of the correlation length L_c). B. Schematic representation the outcome of training the 3D PixelCNN model: a conditional probability of the grid-point X_i given the context of size L_c : $P(X_i | \text{molecular context})$. C. The outcome of the generation process: a sample molecular configuration with dimensions that exceed the dimensions of the training set.

Finally, it is important to discuss whether the generated structures are physical. We showed in Ref.¹⁴ that MAP-generated structure can be thought of as a converging Markov chain that is guaranteed to realize a unique steady-state distribution (the distribution of the small-scale samples used in training) and the extrapolation scheme in the MAP is physically motivated by the decaying correlation length in amorphous or strongly-disordered materials. Therefore, the generation process can be systematically improved/converged through the tuning of various hyperparameters, and through the design of the training set. Approaches that resemble the MAP have recently emerged based on generative adversarial networks^{19–21}, but to the best of our knowledge so far the physicality of the generated samples has not been systematically explored.

In this paper we present an implementation of the MAP for the simulation of 3D multi-element atomistic molecular structures. This was a challenging step forward which succeeded against expectations without any modifications to the essence of the protocol or to the representation of molecular structures pointing to the strengths of the MAP, and to the excellent performance of PixelCNN on extremely sparse datasets. The sparsity in our case is due to the fact that molecules are represented as collections of points corresponding to centers of atoms in discretized real space (without any information about chemical bonds or distribution of electronic density) which leaves the vast majority of grid-points empty.

To demonstrate the performance of multi-elemental MAP in 3D we use liquid water as model system. Water has various anomalous properties that have been of great interest for more than five decades^{22,23}. Here we first verify that our model successfully generates liquid water in

ambient conditions and then turn our attention to a more challenging scenario - the problem of ice nucleation. The onset of ice nucleation is a rare event and it is studied computationally by enhanced sampling methods such as Umbrella sampling²⁴⁻²⁸, Metadynamics^{29,30} and Transition Path Sampling^{31,32}. These methods are computationally expensive in general as they need to sample over many possible configurations and restrict the nucleation process to highly metastable conditions. Recently seeding approaches^{33,34} provided an alternative framework. In this method, a crystalline cluster is inserted in the supercooled fluid and the fluid molecules that overlap with the seeded cluster are removed. In seeded simulation approach, important quantities to describe nucleation such as barrier height, nucleation rate or interfacial free energy can be found, with a moderate computation effort. This means systems where the critical nucleus consists of several thousands of particles can also be studied. However, due to the nature of this approximation technique and its nonquantifiable artifacts obtaining accurate nucleation rate observed in experiments³⁵ has been challenging. Using the MAP we explore the possibility to sample rare configurations that may be difficult to access using traditional techniques by generating a sample with a small ice nucleus such that the surrounding water molecules are sampled from a distribution conditional on the presence of this extremely rare motif³⁶ thereby producing perhaps improved initial conditions for the seeding simulation.

In this paper, we present the 3D multi-elemental implementation of the MAP and our first proof-of-concept application of the MAP to water. At this stage, we measure success based on the stability of the traditional simulations seeded with the MAP-generated initial conditions and the preliminary evaluation of the physicality of results, and we leave a deeper physical exploration of the results of these trajectories to future work. The paper is organized as follows: in Methodology section we present the details of the MAP and its multi-elemental implementation in 3D and the technical details of the molecular dynamics simulations, Results and Discussion section discusses the MAP performance on liquid water dataset and the results of molecular dynamics simulations seeded with configurations generated by the MAP, Conclusions provide an executive summary and outlook.

METHODOLOGY

1. The Morphological Autoregression Protocol (MAP).

For the detailed presentation of the MAP, we refer the reader to two previous reports where the MAP methodology is presented¹³ and analyzed¹⁴. Here we only present a terse summary of the approach and the details of the implementation in 3D. In this approach, the space is discretized, and the molecular structure is viewed as a sequence $\{X\}$. The probability that grid point i is occupied by a molecular fragment class θ (atomistic or otherwise) is generically given by

$$\text{Equation 1: } P(X_i = \theta | \{X_{j < i}\}) = N[c_{b,\theta} + F_\theta(\{X_{j < i}\})]$$

with $\{\theta \in \mathbb{Z}^+ | \theta \leq N_c\}$ where N_c is the total number of classes, $c_{b,\theta}$ is a linear bias, $F_\theta(\{X\})$ is a function that captures the correlations between X_i and the surrounding structure $\{X_{j < i}\}$ and $N[y]$ signifies the soft-max class-wise normalization function that translates $\mathbf{y}_{\theta,i} \equiv c_b + F_\theta(\{X_{j < i}\})$, into the probabilities for atomic/molecular structures expected at grid-point i (with $\beta = 1$):

$$\text{Equation 2: } N[y_{\theta,i}] = \frac{e^{\beta y_{\theta,i}}}{\sum_{\theta} e^{\beta y_{\theta,i}}}.$$

With index i running over multiple dimensions, one can generate 1, 2 or 3 dimensional sequences corresponding to 1D, 2D, and 3D materials. Uniquely, finite morphological correlation lengths in disordered materials allow us to truncate the molecular context at some finite correlation length L_c (Figure 1B) without loss of accuracy, in other words:

$$\text{Equation 3: } \lim_{i \rightarrow \infty} F_{\theta}(\{X_{j < i}\}) = F_{\theta}(\{X_j \in L_c\}).$$

Thereby, the probability for a sequence element to be of class θ is given by

$$\text{Equation 4: } P(X_i = \theta | \{X_{j < i}\}) = N[c_{b,\theta} + F_{\theta}(\{X_j \in L_c\})]:$$

which are normalized, nonzero probabilities for each class, see Equation 2. Sampling this conditional probability starting from either empty space or from some initial conditions will generate the sequence $\{X\}$ element by element with newly generated elements fed back into the conditional probability as part of the structural context $\{X_j \in L_c\}$.

The correlation function F_{θ} in Equation 4 may have different forms depending on the system that is being studied. For systems such as ideal gas, or dilute fluids, one can derive F_{θ} by incorporating pairwise correlations of particles^{14,37}, but this is not a trivial task for dense fluids and similarly for the amorphous materials where one needs to take into account correlations of two pairs, three pairs, one 3-body cluster, one 3-body and one pair, etc., up to large clusters of particles. The number of these terms explodes exponentially with correlation length L_c and size of the aggregates. Therefore, we resort to fitting F_{θ} as accurately as possible using data. In the next section, we describe the PixelCNN model which is known for its effectiveness in learning and generating complex multi-dimensional datasets.

2. PixelCNN:

PixelCNN is a variant of convolutional neural networks which explicitly outputs the conditional probability distribution for all the grid-points in 3D or voxels in an image, $\{X\}$, given the surrounding voxels:

$$\text{Equation 7: } P(\{X\}) = \prod_i^{n_r \cdot n_c \cdot n_l} P(X_i | \{X_{j < i}\}).$$

Here the set $\{X\}$ represents the training data in the sequential form with n_r , n_c and n_l corresponding to the number of rows, columns, layers of the 3D input data. To ensure the receptive field of the convolutions around each target voxel, here with size of 3x3x3, only includes the voxels on which its probability is conditioned (thus, avoiding seeing the future

voxels/context) a mask is added to each convolution, see Figure 3(B).

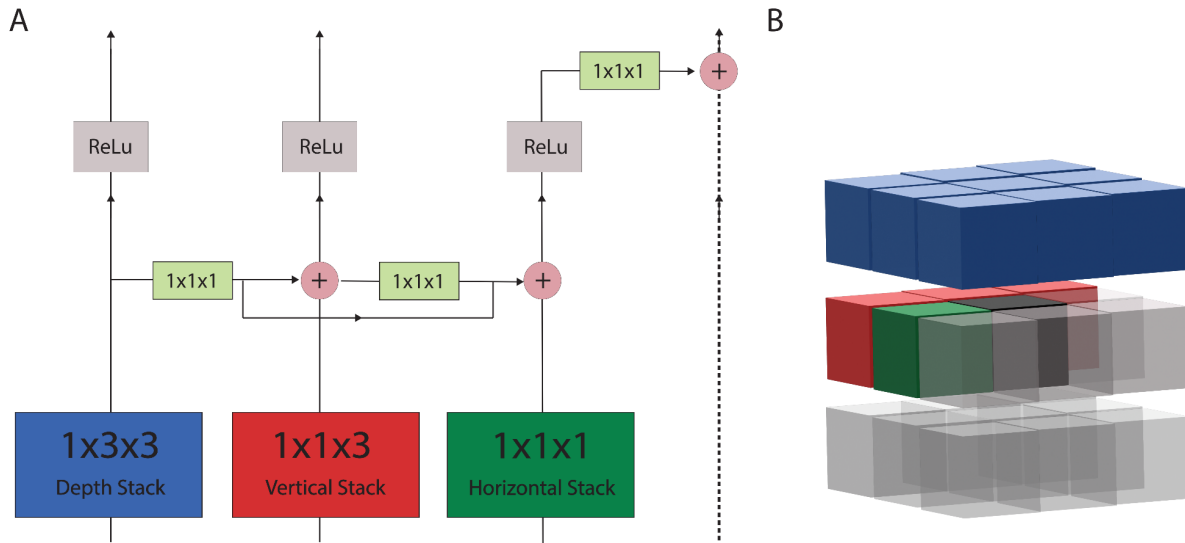


Figure 3: Panel(A) depicts the architecture of PixelCNN in 3D, with stacks working independently to overcome the blind spot problem. Panel(B) Masked kernel (3x3x3) centered on a target voxel (black), the voxels prior to the target voxel are shown in blue, red and green corresponding to the prior voxels being convoluted in depth, vertical, horizontal stacks respectively.

However, the use of ‘masked’ convolutions leads to loss of information, this artifact is known as blind spot. The elimination of the blind spot is achieved by use of two masks - vertical and horizontal¹⁵ in 2D. We extend this approach to 3 dimensions by splitting the masked 3x3x3 convolution into a 1x1x1 (horizontal) and 1x1x3 (vertical) convolution and 1x3x3 (depth) convolution. Thus, these convolutions are done in 3 separated stacks demonstrated in Figure 3 (A). Note that the information from depth stack is flowed to vertical and horizontal, and from vertical to horizontal in a unidirectional manner by 1x1x1 connections. Depth stack should not have access to any information the vertical has, and similarly vertical stack is blind to the information accessible to the horizontal stack, otherwise they would access the voxels that they should not see.

We used Rectified Linear Units (ReLU) activations for each layer. As in Ref¹⁵, after the first layer we add a residual connection from the ReLU unit in horizontal to the output of the next one. Moreover, the final convolution is accompanied by dropout, a well-known regularization method³⁸, to increase the network generalizability. In the generation phase, the softmax operation is followed by multinomial sampling using the normalized voxels probabilities, to predict the voxel value. This step is the implementation of Equation 4 described in the MAP protocol. The predictions for each voxel are compared with the associated voxel value in training sample by using a cross-entropy loss function per-voxel defined as:

$$L_{CE} = - \sum_{\theta} t_{\theta} \log P(X_i = \theta)$$

Where t_{θ} is the one-hot encoded truth value of each voxel, and $P(X_i = \theta)$ is the prediction made by Equation 4. Finally, a backpropagation algorithm is performed by using the computed loss function for every batch of training sample to update the parameters of the model.

3. Molecular dynamics simulations

The classical molecular dynamics (MD) and quantum mechanical path integrals MD (PIMD) simulations were performed at 300 K and 230 K for pure water and 230 K for seeded ice using samples with a total of 343 water molecules. Periodic boundary conditions were applied using the minimum image convention. First a NPT equilibration was done for 125 ps, followed by a NVT run for 500 ps at 1 bar using an Andersen thermostat and an anisotropic Berendsen barostat, respectively^{39,40}. For all calculations the q-TIP4P/05 water potential of Habershon et al.⁴¹ has been used. Short-range interactions were truncated at 10 Angstrom and Ewald summation was employed to calculate the long-range electrostatic interactions. We used discrete time steps of 0.5 fs for the intermolecular and 0.1 fs for the intramolecular forces⁴². For the PIMD calculations the ring polymer contraction scheme with a cut-off value of $\sigma = 5$ Angstrom was employed to reduce the electrostatic potential energy and force evaluations to a single Ewald sum, speeding up the calculations⁴³. 32 beads were used, contracting to a centroid for the computational expensive part of the electrostatic interactions. Ensemble averages were calculated over the whole trajectory length of 500 ps. The training set was generated using a PIMD trajectory (i.e., including nuclear quantum effects) sampled at 1.25 ps rate to make a total of 1000 decorrelated configurations of 216 water molecules⁴⁴.

RESULTS AND DISCUSSION

1. Liquid Water: For training on liquid water structures, 1000 samples were generated by PIMD simulations (see Methods for details). We augmented this dataset with samples rotated 90 and 180 degrees in each direction to achieve a training set containing 7000 samples with volume of 80x80x80 voxels. Each voxel is equal to 0.25\AA^3 introducing an average distortion in atom positions of 4 % of O-H covalent bond length upon discretization of space. Finally, to reduce the memory usage, we subsampled each configuration with 8 equally sized and non-overlapping samples, this leads to 56000 40x40x40voxels samples. This data set was split 80:20 into training and test data sets. We chose model architecture with 20 layers each having 20 convolutional kernels. Stochastic gradient descent (SGD) with momentum of 0.9 was used, and the training was done using cross entropy loss function and stopped after 493 epochs with the batch size set to 1 and the learning rate to 0.01. A dropout with probability of 0.21 was used after the final layer which randomly sets to zero one of the elements of the features tensor.

Figure 4 shows results and compares the accuracy metrics computed on the training samples to those generated by our model. For this comparison we have generated one sample with dimensions of 160x160x160 voxels or $4\text{x}4\text{x}4\text{ nm}^3$, i.e., each side was twice as large as the training data samples, for an illustration, see Figure 4B. The overall comparison demonstrates strong performance with excellent agreement between the training and the generated samples. We use element-resolved radial distribution function to evaluate agreement: see Figure 4C for

Oxygen-Oxygen RDF, Figure 4D for H-H RDF, and Figure 4E for O-H RDF. The radial distribution function $g(r)$ function was calculated by counting the number of particles contained in a volume within the spheres of radii r and $r + dr$ away from a reference particle. As the training samples and outputs are in the discretized space, dr was chosen to be half of voxel side (0.125\AA). Note that this discretization gives rise to the noisy RDFs in Figure 4. To account for normalization, the counts in previous step were divided by $\rho 4\pi r^2 dr$, where ρ is the number density. Finally, we note that the model captures the water bond angle (Figure 4F) and bond lengths (Figure 4G) very well.

In order to use the output of our model in molecular dynamics simulations, we have generated a sample with dimensions of $24 \times 24 \times 24$ voxels that includes 343 water molecules and used it as initial configuration in a set of classical MD and quantum mechanical PIMD simulations. The results of these simulations are discussed in part 3 of this section.

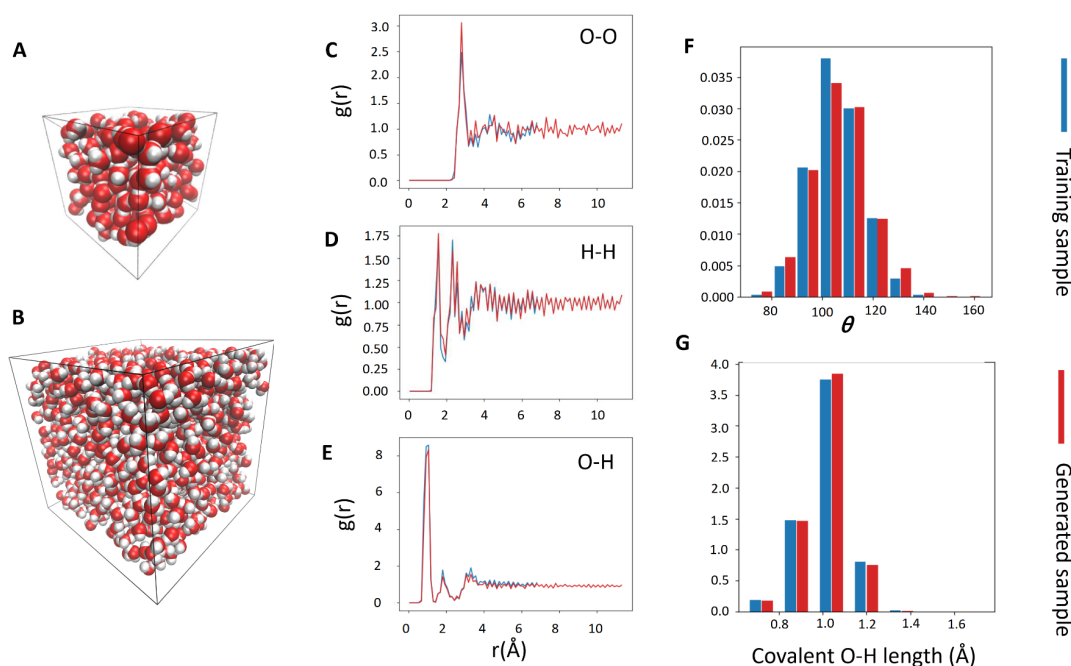


Figure 4: Results from the MAP trained on an ambient liquid water dataset. Panel A shows a sample from the training set and panel B shows a generated sample. Panels C, D and E give the radial pair correlations for O-O, H-H, and O-H, and F, G show distributions of H-O-H bond angles and covalent O-H bond lengths.

We note that in spite of strong performance, our model is prone to minor mistakes leaving oxygens and hydrogens ‘orphan’ in rare cases. The number of these defects are less than 0.5 %, in total 88 among 1923 generated water molecules with majority found at the boundaries. This is expected since we fix the number of voxels in the generated sample rather than the number of molecules and molecules initiated at the edges do not get completed. These defects can be removed with a simple post-processing step.

2. *Configurations with Seeded Ice:* As a case study, we investigate the liquid water configurations in the presence of a seeded ice. We generate such structures in several steps: (i) initialize an empty sample with a small cubic ice configuration and generate its surrounding grid-points with our model trained on the liquid water, see Figure 5(A); (ii) we rotate the generated sample anti-clockwise along the z (blue axis) and clockwise along the x direction (red axis); (iii) we now populate the grid-points that remained empty after step (i), see Figure 5(B). Consequently, we have a sample with an ice nucleus in the center of the box and water molecules around it sampled from a distribution that was conditioned on the presence of ice, Figure 5(C). The ice nucleus contains 103 molecules, and a sample is generated with 343 water molecules in total (including the ice molecules). As before we use this configuration to initiate molecular dynamics simulations, see the discussion in part 3 of Results and Discussion.

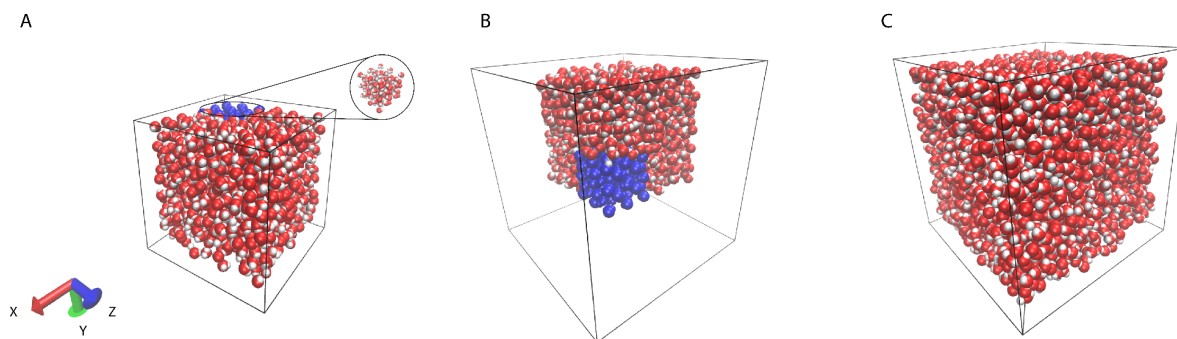


Figure 5: Panel A shows the generation of water liquids around ice nucleus (blue molecules) seeded in the corner of the box. Panel B shows the rotated configuration in Panel A with empty space that is filled in Panel C. As a result, the ice cube is placed in the center of the box surrounded with water molecules.

3. *Molecular dynamics simulations*

In order to put the MAP-generated configurations to a test we ran several molecular dynamics trajectories and kept track of the physicality of observables. Two sets of simulations were performed: classical MD and quantum mechanical PIMD simulations including nuclear quantum effects (NQE). The results are summarized in Figure 6 and Table 1.

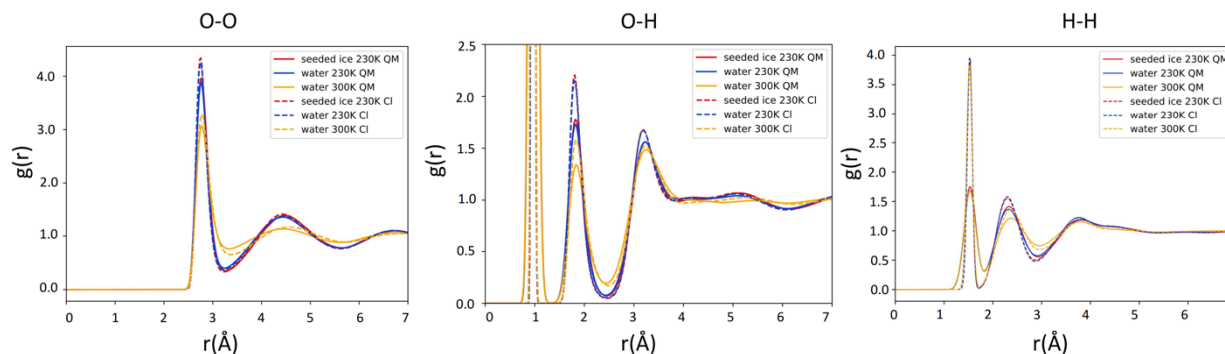


Figure 6: Oxygen-oxygen (left), oxygen-hydrogen (middle), and hydrogen-hydrogen (right)

Radial Distributions Function (RDF) for water at 300 K (blue), supercooled water at 230 K (red) and water seeded with ice at 230 K (orange) classical (dotted) and with NQE (solid). All calculated RDFs are computed from 10000 steps from quantum mechanical PIMD including nuclear quantum effects (NQE) with 250 ps length and 20000 steps of classical path integrals molecular dynamics (PIMD) calculation with a total length of 500 ps.

Overall, the water at ambient temperature shows the typical behavior we would expect, similar to experimental and theoretical studies done before⁴⁵⁻⁴⁷. The O-O, O-H and H-H radial distribution functions (RDFs) for the classical and the quantum simulations are shown in Figure 6, and they show very similar structures. No nucleation of ice in MD/PIMD calculations of this length can be observed⁴⁶. As summarized in Table 1, classical water at 300 K had an average density of 1.003 g/cm³, average intramolecular O-H bond length of 0.9623 Å, average bond angle of 140.739 degrees and average dipole of 2.308 Debye. This shows that using MAP-generated starting structures reproduce generally accepted values for calculating water properties⁴⁸.

	Density [g/cm ³]	Average O-H bond length [Å]	Average bond angle [degrees]	Average dipole [Debye]
Water 300 K MD	1.0003	0.9623	140.825	2.308
Water 300 K PIMD	0.9958	0.9779	104.710	2.347
Water 230 K MD	0.9906	0.9652	104.872	2.314
Water 230 K PIMD	0.9943	0.9802	104.780	2.351
Seeded Ice 230 K MD	0.9893	0.9653	104.858	2.314
Seeded Ice 230 K PIMD	0.9575	0.9800	104.792	2.350
Experimental water 300 K	0.997	0.97	105.100	2.9

Table 1: Density and average observables over the NPT followed by NVT runs for classical and quantum molecular calculations. Experimental data taken from Ref. ⁴⁵.

Going beyond the confirmation of successful performance of the MAP on the water dataset, we include a brief discussion of our observations in this set of simulations. We notice that the starting densities for classical supercooled water at 230 K and seeded ice at 230 K were calculated at 0.990 g/cm³ and 0.989 g/cm³ respectively. There is a possibility that the seeded ice sample has lost structure in classical equilibration, which would cause similarity in densities. Interestingly, in PIMD simulations there is a large difference in density between the supercooled water at 230 K at 0.9943 g/cm³ and the water with seeded ice at 230K at 0.957 g/cm³. This

difference in density could mean that the amorphous ice geometry still exists in the simulations which include NQE despite most observables from Table 1 being similar. As structures generated by the MAP already include NQE it would be expected that starting molecular dynamics calculation with NQE should have a higher chance of retaining created geometries and shorter trajectories may suffice for the study of ice nucleation removing the need for long (hundreds of nanoseconds) simulations³⁶. However, our goal here is to evaluate the performance of the MAP-generated structures in molecular dynamics simulations, and we leave the exploration of the onset of nucleation around the seeded ice to future work.

CONCLUSIONS

In this paper we have extended to 3D and multi-elemental datasets the morphological autoregressive protocol (MAP), a novel computational approach to generating strongly disordered morphologies at arbitrary scales based on small-scale training samples. By construction, the MAP can be applied to any molecular dataset with sufficiently quickly decaying structural correlation function. Here, we have demonstrated stable performance using water as a system and highlighted the aspects in which the MAP can benefit computational exploration: 1. NQE are naturally included in the generated morphologies by virtue of their inclusion in the training data. This is important for low temperature simulations where water is a quantum liquid because geometries caused by quantum effects that occur in quantum mechanical PIMD simulations do not occur in conventional classical MD simulation; 2. MAP-generated initial conditions may be used to bypass an expensive part of (PI)MD simulation to grow a critically large cluster for ice nucleation by creating water (including NQEs) around cubic ice. We expect this deep learning protocol to be of use in a wide range of computational explorations of strongly disordered materials by providing cost-effective and direct ways of probing the morphological complexity, gaining access to important rare configurations, as well as bridging the gap between the nano- and the meso- scale simulations of molecular configurations.

References

- (1) Lewis, L. J. Fifty Years of Amorphous Silicon Models : The End of the Story? *Journal of Non-Crystalline Solids* **2022**, *580*, 121383. <https://doi.org/10.1016/j.jnoncrysol.2021.121383>.
- (2) Gallo, P.; Amann-Winkel, K.; Angell, C. A.; Anisimov, M. A.; Caupin, F.; Chakravarty, C.; Lascaris, E.; Loerting, T.; Panagiotopoulos, A. Z.; Russo, J.; Sellberg, J. A.; Stanley, H. E.; Tanaka, H.; Vega, C.; Xu, L.; Pettersson, L. G. M. Water: A Tale of Two Liquids. *Chem. Rev.* **2016**, *116* (13), 7463–7500. <https://doi.org/10.1021/acs.chemrev.5b00750>.
- (3) Zhou, Y.; Fan, H. J. Progress and Challenge of Amorphous Catalysts for Electrochemical Water Splitting. *ACS Materials Lett.* **2021**, *3* (1), 136–147. <https://doi.org/10.1021/acsmaterialslett.0c00502>.
- (4) Toh, C.-T.; Zhang, H.; Lin, J.; Mayorov, A. S.; Wang, Y.-P.; Orofeo, C. M.; Ferry, D. B.; Andersen, H.; Kakenov, N.; Guo, Z.; Abidi, I. H.; Sims, H.; Suenaga, K.; Pantelides, S. T.; Özyilmaz, B. Synthesis and Properties of Free-Standing Monolayer Amorphous Carbon. *Nature* **2020**, *577* (7789), 199–203. <https://doi.org/10.1038/s41586-019-1871-2>.

- (5) Ciccotti, G.; Dellago, C.; Ferrario, M.; Hernández, E. R.; Tuckerman, M. E. Molecular Simulations: Past, Present, and Future (a Topical Issue in EPJB). *The European Physical Journal B* **2022**, *95* (1), 3. <https://doi.org/10.1140/epjb/s10051-021-00249-x>.
- (6) Chen, M.; Yu, T.-Q.; Tuckerman, M. E. Locating Landmarks on High-Dimensional Free Energy Surfaces. *Proceedings of the National Academy of Sciences* **2015**, *112* (11), 3235–3240. <https://doi.org/10.1073/pnas.1418241112>.
- (7) Noé, F.; Olsson, S.; Köhler, J.; Wu, H. Boltzmann Generators: Sampling Equilibrium States of Many-Body Systems with Deep Learning. *Science* **2019**, *365* (6457), eaaw1147. <https://doi.org/10.1126/science.aaw1147>.
- (8) Marrink, S. J.; Risselada, H. J.; Yefimov, S.; Tieleman, D. P.; de Vries, A. H. The MARTINI Force Field: Coarse Grained Model for Biomolecular Simulations. *J Phys Chem B* **2007**, *111* (27), 7812–7824. <https://doi.org/10.1021/jp071097f>.
- (9) Pak, A. J.; Voth, G. A. Advances in Coarse-Grained Modeling of Macromolecular Complexes. *Curr Opin Struct Biol* **2018**, *52*, 119–126. <https://doi.org/10.1016/j.sbi.2018.11.005>.
- (10) Husic, B. E.; Charron, N. E.; Lemm, D.; Wang, J.; Pérez, A.; Majewski, M.; Krämer, A.; Chen, Y.; Olsson, S.; de Fabritiis, G.; Noé, F.; Clementi, C. Coarse Graining Molecular Dynamics with Graph Neural Networks. *J. Chem. Phys.* **2020**, *153* (19), 194101. <https://doi.org/10.1063/5.0026133>.
- (11) Botu, V.; Batra, R.; Chapman, J.; Ramprasad, R. Machine Learning Force Fields: Construction, Validation, and Outlook. *J. Phys. Chem. C* **2017**, *121* (1), 511–522. <https://doi.org/10.1021/acs.jpcc.6b10908>.
- (12) Gkeka, P.; Stoltz, G.; Barati Farimani, A.; Belkacemi, Z.; Ceriotti, M.; Chodera, J. D.; Dinner, A. R.; Ferguson, A. L.; Maillet, J.-B.; Minoux, H.; Peter, C.; Pietrucci, F.; Silveira, A.; Tkatchenko, A.; Trstanova, Z.; Wiewiora, R.; Lelièvre, T. Machine Learning Force Fields and Coarse-Grained Variables in Molecular Dynamics: Application to Materials and Biological Systems. *J. Chem. Theory Comput.* **2020**, *16* (8), 4757–4775. <https://doi.org/10.1021/acs.jctc.0c00355>.
- (13) Kilgour, M.; Gastellu, N.; Hui, D. Y. T.; Bengio, Y.; Simine, L. Generating Multiscale Amorphous Molecular Structures Using Deep Learning: A Study in 2D. *J. Phys. Chem. Lett.* **2020**, *11* (20), 8532–8537. <https://doi.org/10.1021/acs.jpcclett.0c02535>.
- (14) Kilgour, M.; Simine, L. Inside the Black Box: A Physical Basis for the Effectiveness of Deep Generative Models of Amorphous Materials. *Journal of Computational Physics* **2022**, *452*, 110885. <https://doi.org/10.1016/j.jcp.2021.110885>.
- (15) van den Oord, A.; Kalchbrenner, N.; Espeholt, L.; Kavukcuoglu, Koray; Vinyals, O.; Graves, A. Conditional Image Generation with PixelCNN Decoders. In *Advances in Neural Information Processing Systems*; Lee, D., Sugiyama, M., Luxburg, U., Guyon, I., Garnett, R., Eds.; Curran Associates, Inc., 2016; Vol. 29.
- (16) Aäron van den Oord; Nal Kalchbrenner; Koray Kavukcuoglu. Pixel Recurrent Neural Networks. In *Proceedings of The 33rd International Conference on Machine Learning*; Maria Florina Balcan, Kilian Q. Weinberger, Eds.; PMLR, 2016; Vol. 48, pp 1747–1756.

- (17) Garzón-Ramírez, A. J.; Gastellu, N.; Simine, L. Optoelectronic Current through Unbiased Monolayer Amorphous Carbon Nanojunctions. *J. Phys. Chem. Lett.* **2022**, *13* (4), 1057–1062. <https://doi.org/10.1021/acs.jpcclett.1c03981>.
- (18) Gastellu, N.; Kilgour, M.; Simine, L. Electronic Conduction through Monolayer Amorphous Carbon Nanojunctions. *J. Phys. Chem. Lett.* **2022**, *13* (1), 339–344. <https://doi.org/10.1021/acs.jpcclett.1c03769>.
- (19) Comin, M.; Lewis, L. J. Deep-Learning Approach to the Structure of Amorphous Silicon. *Phys. Rev. B* **2019**, *100* (9), 094107. <https://doi.org/10.1103/PhysRevB.100.094107>.
- (20) Ryczko, K.; Darancet, P.; Tamblyn, I. Inverse Design of a Graphene-Based Quantum Transducer via Neuroevolution. *J. Phys. Chem. C* **2020**, *124* (48), 26117–26123. <https://doi.org/10.1021/acs.jpcc.0c06903>.
- (21) Mills, K.; Casert, C.; Tamblyn, I. Adversarial Generation of Mesoscale Surfaces from Small-Scale Chemical Motifs. *J. Phys. Chem. C* **2020**, *124* (42), 23158–23163. <https://doi.org/10.1021/acs.jpcc.0c06673>.
- (22) Speedy, R. J.; Angell, C. A. Isothermal Compressibility of Supercooled Water and Evidence for a Thermodynamic Singularity at -45°C . *J. Chem. Phys.* **1976**, *65* (3), 851–858. <https://doi.org/10.1063/1.433153>.
- (23) Angell, C. A.; Sichina, W. J.; Oguni, M. Heat Capacity of Water at Extremes of Supercooling and Superheating. *J. Phys. Chem.* **1982**, *86* (6), 998–1002. <https://doi.org/10.1021/j100395a032>.
- (24) Rein ten Wolde, P.; Ruiz-Montero, M. J.; Frenkel, D. Numerical Calculation of the Rate of Crystal Nucleation in a Lennard-Jones System at Moderate Undercooling. *J. Chem. Phys.* **1996**, *104* (24), 9932–9947. <https://doi.org/10.1063/1.471721>.
- (25) Torrie, G. M.; Valleau, J. P. Nonphysical Sampling Distributions in Monte Carlo Free-Energy Estimation: Umbrella Sampling. *Journal of Computational Physics* **1977**, *23* (2), 187–199. [https://doi.org/10.1016/0021-9991\(77\)90121-8](https://doi.org/10.1016/0021-9991(77)90121-8).
- (26) Brukhno, A. V.; Anwar, J.; Davidchack, R.; Handel, R. Challenges in Molecular Simulation of Homogeneous Ice Nucleation. *Journal of Physics: Condensed Matter* **2008**, *20* (49), 494243. <https://doi.org/10.1088/0953-8984/20/49/494243>.
- (27) van Duijneveldt, J. S.; Frenkel, D. Computer Simulation Study of Free Energy Barriers in Crystal Nucleation. *J. Chem. Phys.* **1992**, *96* (6), 4655–4668. <https://doi.org/10.1063/1.462802>.
- (28) Torrie, G. M.; Valleau, J. P. Monte Carlo Free Energy Estimates Using Non-Boltzmann Sampling: Application to the Sub-Critical Lennard-Jones Fluid. *Chemical Physics Letters* **1974**, *28* (4), 578–581. [https://doi.org/10.1016/0009-2614\(74\)80109-0](https://doi.org/10.1016/0009-2614(74)80109-0).
- (29) Trudu, F.; Donadio, D.; Parrinello, M. Freezing of a Lennard-Jones Fluid: From Nucleation to Spinodal Regime. *Phys. Rev. Lett.* **2006**, *97* (10), 105701. <https://doi.org/10.1103/PhysRevLett.97.105701>.
- (30) Laio, A.; Parrinello, M. Escaping Free-Energy Minima. *Proceedings of the National Academy of Sciences* **2002**, *99* (20), 12562–12566. <https://doi.org/10.1073/pnas.202427399>.

- (31) Bolhuis, P. G.; Chandler, D.; Dellago, C.; Geissler, P. L. TRANSITION PATH SAMPLING: Throwing Ropes Over Rough Mountain Passes, in the Dark. *Annu. Rev. Phys. Chem.* **2002**, *53* (1), 291–318. <https://doi.org/10.1146/annurev.physchem.53.082301.113146>.
- (32) Lechner, W.; Dellago, C.; Bolhuis, P. G. Role of the Prestructured Surface Cloud in Crystal Nucleation. *Phys. Rev. Lett.* **2011**, *106* (8), 085701. <https://doi.org/10.1103/PhysRevLett.106.085701>.
- (33) Espinosa, J. R.; Vega, C.; Valeriani, C.; Sanz, E. Seeding Approach to Crystal Nucleation. *J. Chem. Phys.* **2016**, *144* (3), 034501. <https://doi.org/10.1063/1.4939641>.
- (34) Sanz, E.; Vega, C.; Espinosa, J. R.; Caballero-Bernal, R.; Abascal, J. L. F.; Valeriani, C. Homogeneous Ice Nucleation at Moderate Supercooling from Molecular Simulation. *J Am Chem Soc* **2013**, *135* (40), 15008–15017. <https://doi.org/10.1021/ja4028814>.
- (35) Zimmermann, N. E. R.; Vorselaars, B.; Quigley, D.; Peters, B. Nucleation of NaCl from Aqueous Solution: Critical Sizes, Ion-Attachment Kinetics, and Rates. *J. Am. Chem. Soc.* **2015**, *137* (41), 13352–13361. <https://doi.org/10.1021/jacs.5b08098>.
- (36) Matsumoto, M.; Saito, S.; Ohmine, I. Molecular Dynamics Simulation of the Ice Nucleation and Growth Process Leading to Water Freezing. *Nature* **2002**, *416* (6879), 409–413. <https://doi.org/10.1038/416409a>.
- (37) Schreiber, F.; Zanini, F.; Roosen-Runge, F. Viral Expansion- A Brief Introduction. **2011**.
- (38) Srivastava, N.; Hinton, G.; Krizhevsky, A.; Sutskever, I.; Salakhutdinov, R. Dropout: A Simple Way to Prevent Neural Networks from Overfitting. *J. Mach. Learn. Res.* **2014**, *15* (1), 1929–1958.
- (39) Tuckerman, M.; Berne, B. J.; Martyna, G. J. Reversible Multiple Time Scale Molecular Dynamics. *J. Chem. Phys.* **1992**, *97* (3), 1990–2001. <https://doi.org/10.1063/1.463137>.
- (40) Andersen, H. C. Molecular Dynamics Simulations at Constant Pressure and/or Temperature. *J. Chem. Phys.* **1980**, *72* (4), 2384–2393. <https://doi.org/10.1063/1.439486>.
- (41) Habershon, S.; Markland, T. E.; Manolopoulos, D. E. Competing Quantum Effects in the Dynamics of a Flexible Water Model. *J. Chem. Phys.* **2009**, *131* (2), 024501. <https://doi.org/10.1063/1.3167790>.
- (42) Berendsen, H. J. C.; Postma, J. P. M.; van Gunsteren, W. F.; DiNola, A.; Haak, J. R. Molecular Dynamics with Coupling to an External Bath. *J. Chem. Phys.* **1984**, *81* (8), 3684–3690. <https://doi.org/10.1063/1.448118>.
- (43) Markland, T. E.; Manolopoulos, D. E. A Refined Ring Polymer Contraction Scheme for Systems with Electrostatic Interactions. *Chemical Physics Letters* **2008**, *464* (4), 256–261. <https://doi.org/10.1016/j.cplett.2008.09.019>.
- (44) John, C.; Spura, T.; Habershon, S.; Kühne, T. D. Quantum Ring-Polymer Contraction Method: Including Nuclear Quantum Effects at No Additional Computational Cost in Comparison to Ab Initio Molecular Dynamics. *Phys. Rev. E* **2016**, *93* (4), 043305. <https://doi.org/10.1103/PhysRevE.93.043305>.

- (45) Soper, A. K. The Radial Distribution Functions of Water and Ice from 220 to 673 K and at Pressures up to 400 MPa. *Chemical Physics* **2000**, *258* (2), 121–137. [https://doi.org/10.1016/S0301-0104\(00\)00179-8](https://doi.org/10.1016/S0301-0104(00)00179-8).
- (46) Vega, C.; Abascal, J. L. F.; Conde, M. M.; Aragoes, J. L. What Ice Can Teach Us about Water Interactions: A Critical Comparison of the Performance of Different Water Models. *Faraday Discuss.* **2009**, *141* (0), 251–276. <https://doi.org/10.1039/B805531A>.
- (47) Li, Y.; Li, J.; Wang, F. Liquid–Liquid Transition in Supercooled Water Suggested by Microsecond Simulations. *Proceedings of the National Academy of Sciences* **2013**, *110* (30), 12209–12212. <https://doi.org/10.1073/pnas.1309042110>.
- (48) Eltareb, A.; Lopez, G. E.; Giovambattista, N. Nuclear Quantum Effects on the Thermodynamic, Structural, and Dynamical Properties of Water. *Phys. Chem. Chem. Phys.* **2021**, *23* (11), 6914–6928. <https://doi.org/10.1039/D0CP04325G>.